MODELING COMPACT NON-VOLATILE PHOTONIC SWITCHING BASED ON OPTICAL PHASE CHANGE MATERIAL AND GRAPHENE HEATER

by

Khoi Phuong Dao

Submitted to the Department of Materials Science and Engineering

in partial fulfillment of the requirements for the degree of

Master of Science in Materials Science and Engineering

at the

MASSACHUSETTS INSTITUTE OF TECHNOLOGY

February 2024

Author ..... Khoi Phuong Dao

Department of Materials Science and Engineering

January 19, 2024

Certified by ..... Juejun Hu

Professor

Thesis Supervisor

Accepted by ..... Robert J. Macfarlane

Professor of Materials Science and Engineering

Chair, Department Committee on Graduate Studies

MODELING COMPACT NON-VOLATILE PHOTONIC SWITCHING BASED ON OPTICAL PHASE CHANGE MATERIAL AND GRAPHENE HEATER

by

Khoi Phuong Dao

Submitted to the Department of Materials Science and Engineering

on January 19, 2024, in partial fulfillment of the

requirements for the degree of

Master of Science in Materials Science and Engineering

Abstract

On-chip photonic switches are the building blocks for programable integrated circuits (PICs) and the integration of phase change materials (PCMs) enables promising designs which are compact, non-volatile, and efficient. However, conventional PCMs such as $Ge_2Sb_2Te_5$ (GST) introduce significant optical absorption loss, leading to elevated insertion losses in devices. Current approaches, compensating for this loss through weak evanescent light-PCM interactions, result in larger footprint devices. A compact non-volatile 2 × 2 switch design is introduced, leveraging optical concentration in slot waveguide modes to significantly enhance interactions of light with PCM, thereby realizing a compact, efficient photonic switch. The crystalline-amorphous phase transitions are driven by an integrated single-layer graphene heater, providing high electro-thermal efficiency, low absorption loss, and rapid switching speed. Computational simulations demonstrate reversible phase transitions of Sb_2Se_3 facilitating 2 working states with crosstalk (CT) down to -24 dB at 1550 nm wavelength and more than 55 nm 0.3 dB insertion loss (IL)bandwidth. The proposed photonic switch architecture can constitute the cornerstone for next-generation high-performance reconfigurable photonic circuits.

Thesis Supervisor: Juejun Hu

Title: Professor

Acknowledgments

First of all, I would like to thank my advisor, Prof. Juejun Hu. He offered me a lot of guidance and creative ideas to complete this project as well as my whole academic period.

I would like to thank Prof. Richard Soref, Prof. Francesco De Leonardis, and Prof. Carlos Ríos for their invaluable technical support and insightful discussion in this project. I would also like to thank everyone in Photonic Materials Group and Electronic Materials Group for giving me help and suggestions. I had great experience working with my group mates.

Finally, I would like to thank my parents, my group mates and my soccer club (Boston Red Lobsters) friends who offered me support and gave me advice in the time of my academic journey.

Contents

List of Figures

List of tables

Chapter 1
Introduction

This chapter introduces the motivation for the project and current challenges that can be solved by the proposed design.

1.1 Background:

In recent decades, the rapid advancement of photonic integrated circuits (PICs) has showcased their potential in telecommunication and data interconnects, primarily due to low-loss broadband transmission capabilities. The evolution of technology, marked by the deceleration of Moore's law[1] and the emergence of the von Neumann bottleneck in electronics, suggests that scalable programmable PICs could offer a viable alternative to electronic systems [2]. Particularly, they could play a pivotal role in energy-efficient broadband classical and/or information storage and quantum computing[3,4] .

Traditional programming approaches for photonic systems have predominantly relied on weak thermo-optic effects [5], free-carrier effects [6], or electro-optic effects [7] within materials. Despite their high-speed capabilities, these mechanisms are constrained by a small change in refractive index ($\Delta n < 0.01$), limiting their tunability and scalability. This limitation results in large device footprints (> 100 μm) and high energy consumption. Although plasmonic effects can reduce device footprints to approximately 10 μm [8], they often lead to lossy devices, rendering them unsuitable for large-scale systems. Moreover, thermo-optic effects introduce significant thermal crosstalk, necessitating additional heaters and control circuits for compensation. Notably, these effects are volatile and demand a constant power supply (~10 mW), requiring infrequent programming [9]. Consequently, traditional metrics like switching speed and switch energy become less crucial due to the infrequent switching events.

To overcome these challenges, addressing alternative active photonic materials with large, non-volatile optical modulation is imperative. Chalcogenide-based phase change materials (PCMs) emerge as promising candidates due to their two stable, reversibly switchable states (amorphous and crystalline), prolonged retention times, and extremely high refractive index contrast ($\Delta n \sim 1$) over a broad spectral range[4,10–12]. These properties facilitate ultra-compact, broadband, and multilevel operations for non-volatile photonic applications without static energy consumption[12–15]. Phase transition in PCMs can be reversibly triggered by ultrashort (up to picoseconds) [16] optical or electrical pulses, suggesting feasibility in applications with high cyclability and low energy requirements. Moreover, PCMs offer compatibility with large scale integration, as they can be conveniently deposited using sputtering [4,13,17] or thermal evaporation [10] onto various photonic integrated circuit (PIC) platforms including silicon and silicon nitride.

1.2 Current challenges proposed solutions:

In spite of these advantages, conventional PCMs such as $Ge_2Se_2Te_5$ (GST) and GeTe display significant absorption in both phases at optical communication wavelengths, limiting their effectiveness in phase shifter – a crucial component of programmable PICs. Recently, there has been a growing interest in wide-bandgap PCMs such as GeSbSeTe (GSST) [18], antimony selenide (Sb_2Se_3), and antimony sulfide (Sb_2S_3) [19,20], as these materials can overcome this absorption issue and offer potential solutions to the challenge. Particularly noteworthy is the exceptional performance of Sb_2Se_3, which exhibits minimal losses at 1550 nm and a substantial index contrast ($\Delta n \approx 0.77$) [19]. These characteristics position Sb_2Se_3 as an optimal phase-change material for applications in programmable photonics within the telecommunication bands.

One essential component in modulation devices involving PCMs is the heating mechanism. Electro-thermal techniques facilitating scalable on-chip integration have been explored in various recent studies, utilizing materials such as metals, transparent conducting oxides (TCOs), doped silicon, and, more recently, graphene. While metals prove effective for free-space reflective devices, they introduce notable optical losses in transmissive or waveguide components. Doped silicon, suitable for integrating PCMs into the silicon-on-insulator platform, poses challenges when applied to Si_3N_4-based

devices or other non-silicon waveguide platforms. TCO heaters, while suitable for visible spectrum devices, encounter heightened optical losses in the infrared. To address these challenges, graphene has emerged as the optimal heating material, offering exceptional thermal and electrical conductivity, versatile integration compatibilities, and remarkable stability [21,22]. Recent theoretical analysis and experimental reports [14,23,24] indicates that graphene heaters exhibit two orders-of-magnitude higher figures of merit for overall performance (heating efficiency and induced loss) than that of doped Si or TCO heaters when applied to PCM switching.

In this thesis, we proposed the design of a compact on-volatile photonic 2 × 2 switch engineered on the silicon-on-isolator (SOI) platform. The proposed design integrates Sb_2Se_3, a wide-bandgap phase-change material (PCM), and a single-layer graphene heater. Leveraging the distinctive properties of Sb_2Se_3, the switch design aims to simultaneously achieve low insertion loss, a compact form factor, high extinction ratio, and zero-static power consumption. To assess the optical and thermal performance, comprehensive simulations were conducted using Lumerical FDTD and Three-dimensional (3D) COMSOL Multiphysics, respectively. In chapter 2, we will discuss in details about the integration of PCMs in photonic devices, especially focusing on the crystallization and amorphization of integrated micro-scale PCMs. Chapter 3 first presents our 2 × 2 switch design and its optical performance benchmark, then follows by quantitative analysis on the feasibility of switching Sb_2Se_3's phase using graphene heater. The final chapter is our conclusion and future work.

Chapter 2

PCM integration and reversible phase switching in photonic devices.

2.1 PCM integration and applications

Chalcogenide phase change materials (PCMs) including $Ge_2Se_2Te_5$ (GST), $Ge_2Sb_2Se_4Te_1$ (GSST), Sb_2Se_3, and Sb_2S_3 represent a class of materials which possess electrical and optical properties shifting drastically when they undergo crystalline-amorphous phase transition. This singular attribute serves as the foundational basis for their widespread adoption in nonvolatile electronic data storage, exemplified by instances such as Intel's Optane^{TM} memories. Building upon this success, the domain of photonics emerges as the subsequent frontier where Phase Change Materials (PCMs) can exert a transformative influence. Notably, recent years have witnessed a burgeoning expansion of research inquiries into PCM-based photonics, encompassing a broad spectrum of applications, including but not limited to optical switching [12,25–27], photonic memory [4], optical computing [5,28–30], active metamaterial/metasurface [31–35], and reflective display [36–39]. The implementation of these optical devices, however, introduces distinctive challenges and requisites that often deviate markedly from those conventionally accommodated in the context of electronic memories.

In numerous photonic applications, PCMs are deposited atop silicon or silicon nitride waveguides, thereby indirectly influencing the modulation of the effective index of the propagating working mode within the devices [4,10,12,13,15]. This approach is motivated by the comparatively high optical loss of GST and GSST rendering them unsuitable as core materials for waveguides. Furthermore, this deposition strategy aligns with established photonic fabrication protocols, particularly those based on the silicon on insulator (SOI) and silicon nitride platforms (Figure 2-1). The integration of PCMs typically follows the fabrication of photonic devices and is commonly accomplished through patterned sputtering or thermal evaporation deposition. However, the indirect

integration configuration in these instances tends to yield less efficient switching mechanisms for PCMs, necessitating prior engineering and fabrication efforts. Commonly employed metal resistive heaters such as Al and Ti/TiN, prevalent in photonic thermal-optical modulation, prove ineffective for PCMs due to the exceedingly high temperatures (exceeding 900K for Sb_2Se_3) required during the amorphization or melt-quenching process. Consequently, doped silicon heaters and 2D-material heaters emerge as more promising alternatives [10,12,15,25,27]. An alternative strategy involves leveraging optical power, where intense light pulses supply energy to the PCMs, inducing crystallization or amorphization [4].

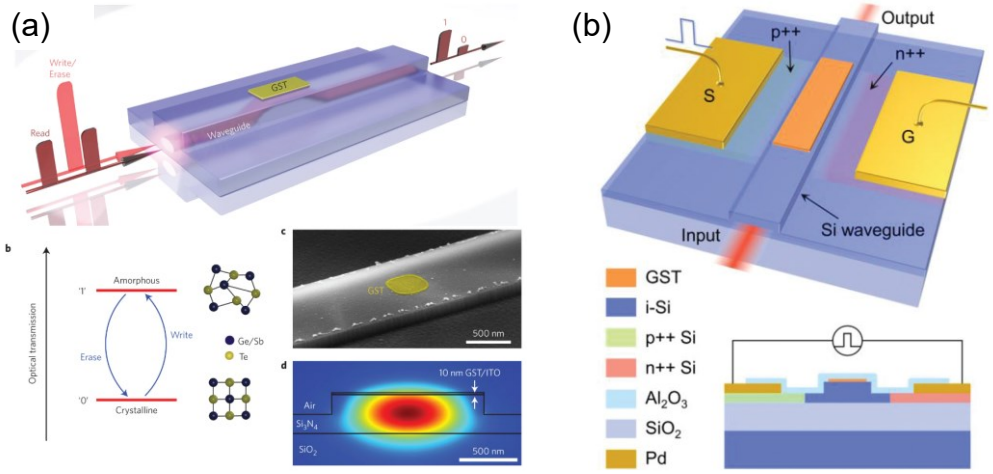

Figure 2-1. PCMs integration scheme on (a) Silicon nitride platform [4], and (b) Silicon-on-insulator platform [15]. The phase transition is triggered by high intensity optical pulse in (a) and electro-thermal pulse in (b).

In recent years, there has been a notable surge in interest and attention directed toward meta-optic and metasurface research, driven by their inherent advantages, including lightweight construction, compact form factor, and cost-effectiveness. The substantial refractive index contrast offered by PCMs plays a pivotal role in enabling the tunability of metalenses, thereby facilitating the development of varifocal metalenses. Notably, PCMs such as GSST have demonstrated compatibility with metasurface design, serving as meta-atom materials with exemplary pattern fidelity [32,33,39]. The integration of PCMs and metasurfaces represents a significant advancement, showcasing that non-mechanical active metasurfaces can attain optical performance comparable to conventional precision bulk optics that involve mechanical moving parts [39].

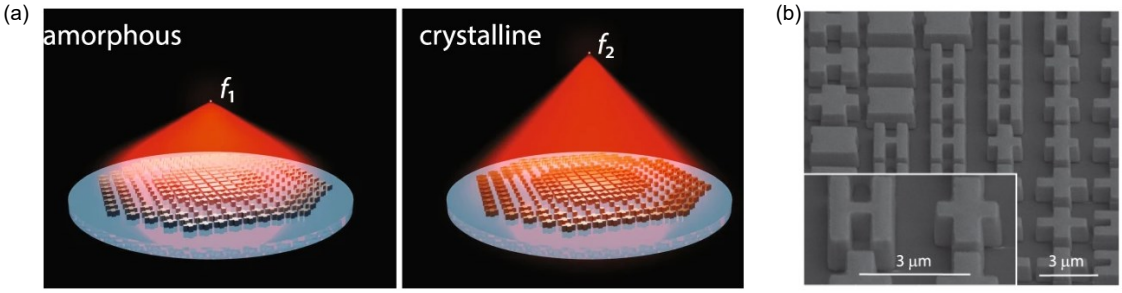

Figure 2-2. Varifocal lens utilizing GSST meta-atoms: (a) working principle, (b) SEM image of GSST meta-atoms [39].

Nonetheless, the application of Phase Change Materials (PCMs) in metasurfaces encounters several challenges, foremost among them being the feasibility of efficiently switching the phase of numerous PCM meta-atoms on an extensive platform. The utilization of integrated heaters, while a common approach, is hindered by challenges related to heat dissipation. This limitation prevents the attainment of a uniform temperature profile [40], a critical requirement for simultaneously crystallizing/amorphizing all atoms across the expansive surfaces of large-area lenses. Consequently, there exists a compelling need for optimization strategies to enhance the integration of PCMs in metasurfaces, addressing the current impediments and advancing the feasibility of realizing uniform and controlled phase transitions across the entire metasurface platform.

The substantial refractive index contrast inherent in PCMs undeniably bestows optical switching with significant advantages. Photonic switches, serving as fundamental components, lay the foundation for the development of scalable and programmable photonic integrated circuits. However, conventional switches, characterized by their weak modulation effects, exhibit drawbacks such as a large footprint and high power consumption. Numerous studies have illustrated that the integration of PCMs with reversible phase switching enables the design of photonic switches with markedly smaller footprints, reduced crosstalk (CT) and insertion loss, and improved speed [12,15,26,27] (Figure 2-3). Moreover, it is reported in several literatures that multilevel electro-thermal switch can be realized by achieving multiple crystallization levels of PCMs through various electro-thermal driven pulse powers [4,24]. However, as mentioned in chapter 1, not all PCMs and heater designs can effectively facilitate the

switch with high performance metric. Sb_2Se_3 and Sb_2S_3 emerge as promising candidates for photonic switches, attributed to their ultralow loss characteristics [19]. However, their elevated melting points pose a challenge to integrated heater designs, necessitating the efficient provision of substantial heat to facilitate phase transitions. The thermal considerations of PCM integration will be explored in greater detail in Section 2.2.

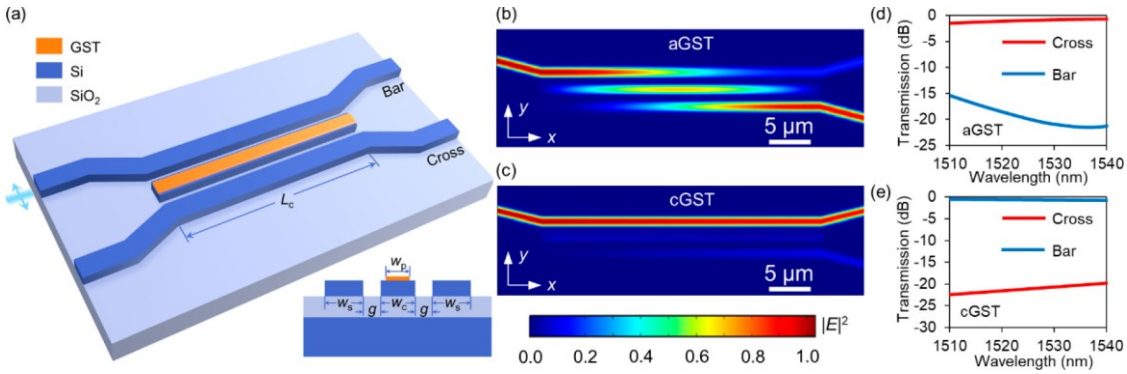

Figure 2-3. 2 × 2 optical switch design utilizing GST [12].

2.2 Crystallization/Amorphization of PCMs in photonic devices and microheater overview

This section is dedicated to investigate integrated heaters, the predominant tools employed in effecting the crystalline-to-amorphous phase transition during the integration of PCMs. These heaters play a pivotal role in toggling the "switch" within integrated optical devices, serving as a means to activate and deactivate the desired states. The process of crystallizing PCMs involves elevating the material's temperature above its crystallization threshold, maintaining this temperature for a specific duration to facilitate the re-localization of atoms into a crystalline structure. Conversely, to induce amorphization in the PCM, the material is heated beyond its liquidus temperature and rapidly quenched to solidify the liquid-like amorphous state. A crucial consideration in these processes is the necessity to kinetically suppress crystallization, achieved by ensuring that the cooling rate surpasses a defined threshold known as the critical cooling rate [19]. This intricate interplay between temperature control and cooling rates is fundamental to the precise modulation of the PCM states, thereby enabling the controlled operation of the integrated optical devices.

Doped silicon heaters emerge as a favorable choice for integrated heating applications due to their compatibility with the silicon-on-insulator (SOI) platform and their capacity

to operate at high temperatures. The utilization of a PIN (p-doped-intrinsic-n-doped) junction, a well-established modulating mechanism in various photonic devices leveraging the electro-optical effect, has been promoted for PCM heating in several studies, highlighting its effectiveness in achieving low-loss modulation [15]. However, challenges arise with the PIN junction approach, as the exceptionally high applied voltage and elevated temperatures during amorphization may lead to junction breakdown, thus, optimization on heater's geometry to maximize heating efficiency is imperative.

In contrast, same-type doped silicon heaters present a more feasible alternative and have demonstrated experimentally viable performance in facilitating PCM phase transitions [10]. Nevertheless, the use of doped silicon slabs introduces considerable optical loss and limits the usable thickness of the working silicon layer. Specifically, in designs employing approximately 100 nm silicon slabs as heating layers, waveguide has to be ridge waveguides, which do not support transverse magnetic (TM) modes. Besides, optimization of doping levels is also imperative to achieve the required heating performance and minimize the induced optical loss. The doping concentration is directly proportional to the propagation loss of the waveguide due to free carrier absorption. Lowering the doping concentration may alleviate the loss issue but require correspondingly high applied voltage to reach the same heating power, which can surpass the CMOS-backend compatible applied voltage maximum. As mentioned previously, temperature uniformity can also raise as a critical issue in large-area doped Si heaters. Due to the considerable heat capacity and finite thermal conductivity, the temperature is usually higher near the center of the heating area and gradually decreases towards the heater boundary. Optimization over heater's geometry to address this issue requires huge computational power and time [41,42]. Another challenge associated doped Si heaters lies in their inherent incompatibility with silicon nitride platform. Consequently, the incorporation of doped silicon heaters onto the silicon nitride platform poses a substantial fabrication burden.

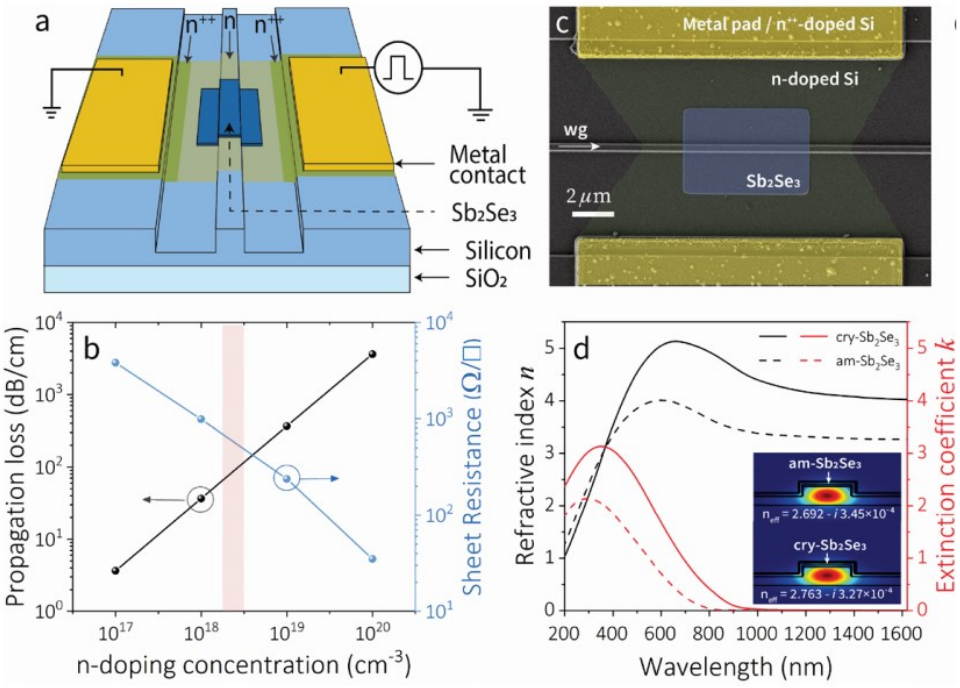

Figure 2-4. Sb_2Se_3 phase shifter using a doped Silicon micro-heater (a) Microheater design in a half-etched 220 nm SOI waveguide. (b) FEM simulated propagation loss and sheet resistivity as a function of phosphorous doping concentration. (c) SEM image of a fabricated 6 µm-long bowtie microheater with a 6 µm-long Sb_2Se_3. (d) Sb_2Se_3 refractive index in both amorphous and crystalline states with simulated optical modes for each state at 1565 nm wavelength [10].

The utilization of 2D heaters, exemplified by Indium Tin Oxide (ITO) heaters or single-layer graphene heaters, presents an alternative avenue for integrated micro-heating mechanisms. These 2D heaters exhibit compatibility with both the silicon-on-insulator (SOI) and nitride platforms. The inherent advantage of these heaters lies in their minimal thickness, which restricts the interaction of the optical mode with the heater, consequently reducing optical losses. Moreover, 2D heaters offer the supplementary benefit of abbreviated cooling times, attributable to their low heat capacity and constrained unwantedly heated regions. Computational simulations have underscored the superiority of graphene heaters and ITO heaters over PIN heaters in Phase Change Materials (PCMs) applications, substantiating their efficacy in achieving enhanced

performance [23].

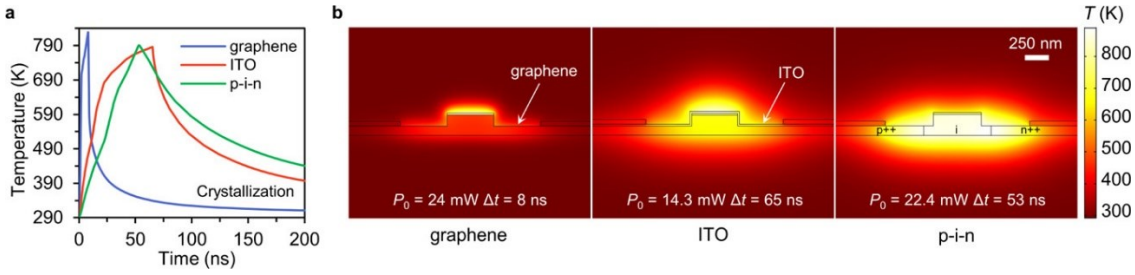

Figure 2-5. (a) Transient temperature response of the phase-change integrated nanophotonic cells (PINCs) with different heaters for crystallization. (b) Temperature distribution at the end of a pulse during the crystallization process in (a) for the PINCs with graphene, ITO, and p−i−n heaters [23]

The thermal treatment plays an important role in PCM integration applications. First, refractive index – the crucial property of PCM – is critically dependent of processing conditions [43]. The discrepancy of optical constant of PCM in amorphous phase is evidently reported in different literature [44], which is directly related the preparation methods and stoichiometry fluctuations-a universal trait of amorphous materials [45]. The property changes of PCM films upon heat treatment, on the other hand, sensitively results in variation of crystalline phase optical constant. The non-uniform heating of PCM during the crystallization would create phase boundary movement, which induces different spatial distribution and phase and different refractive index in comparison with the crystallization through nucleation-dominant regime under uniform temperature condition [46,47]. The dependence of optical constants on heat treatment conditions poses a technical challenge on both optical and thermal designs of PCM devices [43].

Thermal design becomes more critical when we want to optimize the reversible phase switching, which essentially limits the speed the PCM integrated devices. As previously mentioned, the quenching step during the amorphization of PCMs requires a cooling rate surpassing a defined threshold to kinetically impede recrystallization. The dissipation of heat during the quenching step is constrained by a limit on the thickness of the integrated PCM, as it takes time for heat to dissipate from the interior to the surface [43]. This thickness limitation, in turn, compromises the efficacy of modulation in photonic devices configured with a capping layer, thus, the extended path length of the PCM is essential for achieving sufficient light-PCM interaction. The thickness limitation becomes more significant in free space applications exemplified by thin film filters or optical

metasurfaces where a small PCM thickness compromises the modulation range of the phase delay and overall device performance. Beside PCM thickness, the geometry and design of the heater structure directly govern the cooling rate of the PCM. In integrated photonics, the thermal decay time within photonic structures establishes the ultimate limit on switching speed. During the heating phase, not only the PCM but also surrounding materials, such as the silicon waveguide, silicon oxide cladding, and the heater material itself, are heated. Consequently, during the cooling phase, the volume of the heating zone is directly proportional to the thermal decay time. Striking a balance between providing a sufficiently uniform temperature to the targeted PCM and avoiding unnecessary heating of surrounding areas necessitates careful consideration of the heater area. Given that cladding materials generally serve as thermal insulators, achieving an appropriate thickness for the cladding materials is also imperative. Moreover, it is conceivable to enhance the cooling rate by reducing the thermal mass of the heater, for example by using graphene heater instead of doped Si heater [23]. This nuanced approach to thermal design addresses the intricate interplay of factors influencing PCM-integrated devices, offering avenues for optimizing switching speed and overall device performance.

Chapter 3

2x2 photonic switch using Sb_2Se_3 and single-layer graphene heater

3.1 Design and performance benchmark

Figure 3-1 shows the proposed 2 × 2 photonics switch design in a semi-standard SOI platform. The switch consists of a multimode slot waveguide (the two-waveguide coupling zone) attached to four single-mode waveguides serving as input and output ports, connecting either side of the multimode region. From figure 3-1(a), the height and the width of the single-mode waveguides are h = 240 nm and W_{wg} = 450 nm respectively. The slot waveguide has a length L_{slot} = 10 μm and a centrally located slot with a width W_{slot} = 100 nm, which is completely filled with Sb_2Se_3. In the telecommunication C-band, the refractive indices of Sb_2Se_3 are taken from [19] as 3.825 and 4.050 at 1550 nm wavelength for the amorphous Sb_2Se_3 and crystalline Sb_2Se_3 respectively. The loss of crystalline Sb_2Se_3 was also reported in the same paper to be as low as 0.01 dB μm^{-1}. The whole device is cladded by SiO_2. Directly on top of the multimode slot waveguide, there is a single-layer graphene heater. The dimensions of the graphene layer are L_{gr} = 9 μm and W_{gr} = 3 μm and it is symmetrically positioned on the slot waveguide. The metal Ti/Au pads were in contact with the graphene heating layer on each size to minimized the contact resistance. Figure 3-1(b) demonstrate the working principle of the switch as the PCM is switched reversibly by a sequence of voltage pulses applied on the graphene heater. Short pulses (several hundreds of nanoseconds) with high voltage will reset the PCM back to the amorphous state while the long pulses (several milliseconds) with moderate voltage are used to crystallized the material. Sb_2Se_3 was reported to be successfully amorphized at T_m = 620 °C for 400 ns and crystallized at T_c = 200 °C for 10 ms. In this study, the fundamental TE mode at telecommunication wavelength of 1550 nm was targeted as working mode. Yet, the design principle can be applied to broadband device thanks to the wide range of transparency windows of both Sb_2Se_3 and Silicon. The whole design could be realized by conventional electron-beam-lithography (EBL) and dry etching processes. The Sb_2Se_3 and TiO_2 can be deposited in the slot by atomic layer

deposition [48] and solution processing [49]. The graphene heater can be fabricated by transferring chemical-vapor-deposition (CVD) grown single-layer graphene on to Si/SiO_2 wafers by standard wet transfer technique [50]. The graphene can be patterned by EBL, followed by the integration of metal contacts (Ti/Au), which is also pattern by EBL.

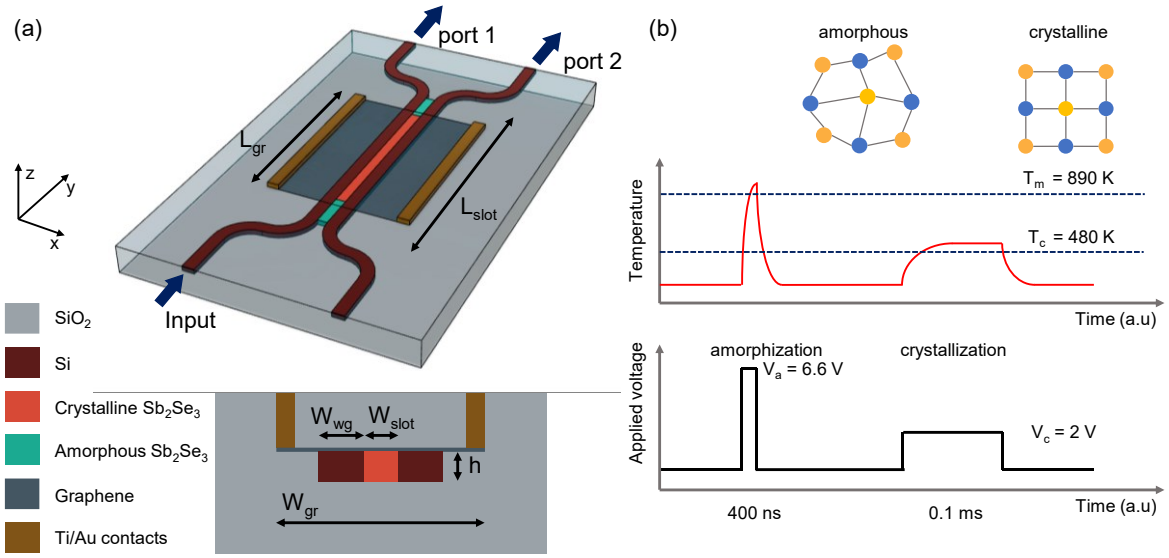

Figure 3-1. (a) Schematic of the 2×2 photonic switch based on Sb_2Se_3 phase switch. (b) Schematic of switching operation utilizing amorphization/crystallization by Joule heating.

The substantial refractive index contrast provided by Sb_2Se_3 facilitates the generation of even and odd TE modes within the multimode slot waveguide, characterized by significant shifts in effective indices upon transitioning the phase of the slot material from amorphous to crystalline states (as depicted in Figure 3-2(a), and 3-2(b)). Exploiting the disparities in the confinement and effective indices of these supermodes at amorphous and crystalline states, the photonic switch can be dynamically shifted from a bar state to a cross state. Due to the difference in propagating constants, the interference between odd mode and even mode results in the oscillation between bar state and cross state when we increase the slot length. Due to the difference in propagating constants, the interference between odd mode and even mode results in the oscillation between bar state and cross state when we increase the slot length. The ultralow loss exhibited by Sb2Se3 allows the PCM to have strong overlap with the supermodes in the slot region without incurring excessive losses, thereby enhancing the phase modulation effect. The effective index differences between the even mode and the odd mode are 0.2951 and 0.3875 for

amorphous and crystalline Sb_2Se_3 states, respectively, corresponding to different beating lengths in the two states.

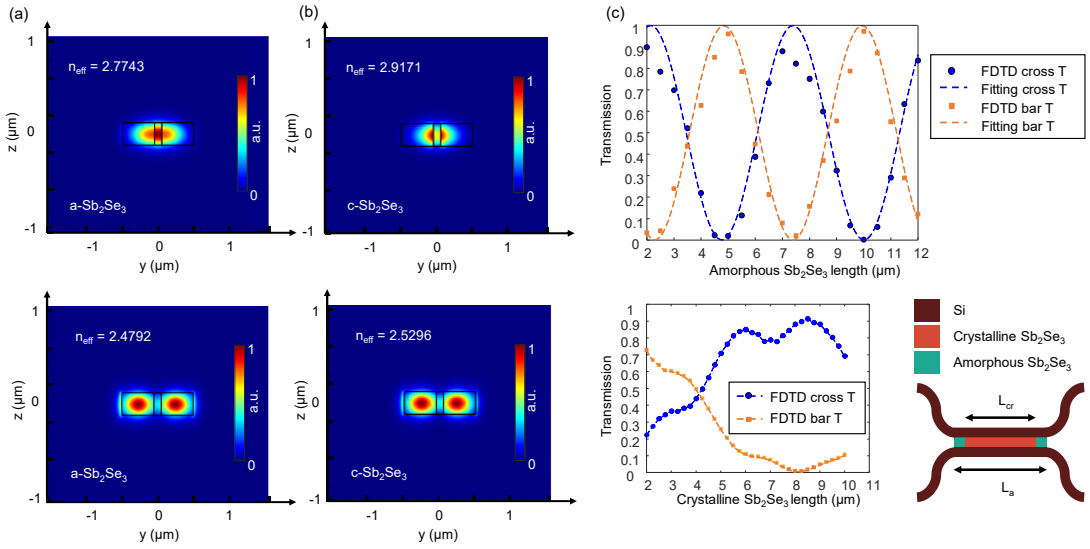

Figure 3-2. (a), (b) The cross-sectional electric field distribution for even and odd TE modes of the multimode slot waveguide, (c) Transmission through the cross port and bar port as functions of PCM length

We conducted 3D FDTD simulations to validate the switching efficiency of our proposed design. Figures 3(a) and 3(b) depict the transmission spectra of our 2 × 2 photonic switch and the corresponding in-plane electric field distributions corresponding to amorphous and crystalline Sb_2Se_3 states. The overall insertion loss (IL) is -0.27 dB (cross state) and -0.11 dB (bar state) at 1550 nm, and is consistently less than 0.5 dB across 1525 nm to 1575 nm wavelengths. The 0.3 dB IL bandwidth is no less than 55 nm. The crosstalk (CT), defined as contrast ratio between the on/off states at the output ports, reaches -23.9 dB (cross state) and -27.4 dB (bar state) at 1550 nm, and stays better than -15 dB throughout the 1525 nm to 1575 nm band. These performance metrics compare favorably to state-of-the-art PCM switches as summarized in Table 1.

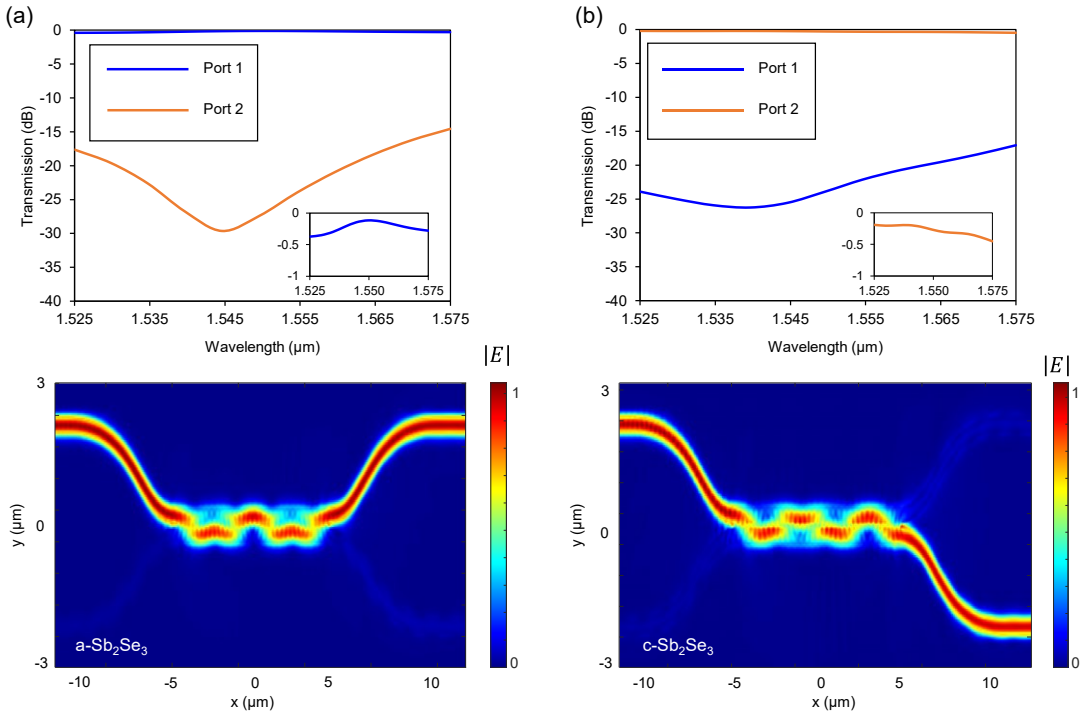

Figure 3-3. Transmission spectra at bar port and cross port and the normalized electric field intensity distribution of the 2 × 2 switch at 1550 nm with (b) amorphous Sb_2Se_3 (b) and crystalline Sb_2Se_3.

Table 3.1. Comparison of PCM-based optical switches

Design	Ref	PCM	IL (dB)	CT (dB)	Footprint (μm^2)	Optical BW (nm)	Switching energy
DC*	[12]	GST	2	-10	5 × 45	30	-
DC*	[17]	GST	2	-10	5 × 50	30	380 nJ (6.8 μJ)
MZI*	[10]	Sb_2Se_3	0.3 [a]	6.5/15	100 × 100	15	176 nJ (3.8 μJ)
MZI*	[51]	Sb_2S_3	3	-12	100 × 100	20	-
MRR	[52]	GST	2	-20	15 × 15	<1	-
MRR*	[53]	GST	3	14	25 × 25	<1	0.25 nJ (11 nJ) [c]
MRR*	[25]	GST	5.1/4.3[b]	5	60 × 60	<1	0.19 nJ (17.1 nJ) [c]
MMI*	[54]	Sb_2Se_3	0.5 [a]	8	6 × 33	-	14 nJ (0.95 mJ)[c]
DC	[27]	Sb_2S_3	0.26	-31.3	4.9 × 25.4	35	9.59nJ (-)
DC	This work	Sb_2Se_3	0.3	-23.9	5.5 × 24	55	21 nJ (1.13μJ)

DC: directional coupler, MZI: Mach-Zehnder Interferometer, MRR: micro-ring resonator, MMI: Multimode Interferometer, IL: insertion loss, CT: crosstalk, Optical BW: optical bandwidth for the corresponding IL, Switching energy: Energy per switching event for amorphization/(crystallization)

*Experimental results

[a] additional loss due to PCMs to the total device IL, [b] through/drop port IL, [c] optical pulse energy

3.2 Feasibility of device – Thermal perspective

To reversibly switch the states of the device depicted in Figure 1, we proposed single-layer graphene heater operated by voltage pulses. Graphene heater has been reported to have outstanding performance as a heating element for integrated photonic devices incorporating PCMs, offering great energy efficiency and high operational speed [14,22,23], owing to its ultralow heat capacity and high in-plane thermal and electrical conductivity. Compared to doped Si, which is another popular choice of heater material, graphene heaters claim significantly lower induced loss and higher heating efficiency [23,24]. The Joule heating employing graphene heater follows similar phase change dynamics demonstrated in Ref [10,24]. The pulse width and voltage are contingent on microheater's properties. With our specific proposed graphene heater, pulses of 2V, which induces a current of 5.67 mA, with duration of 100 μs are applied to partially crystallize the Sb_2Se_3 slot, heating its 8.5 μm long center section to above the crystallization temperature T_c (here set as 200 °C). It is reported that pulses (as short as 5 μs) can crystallize Sb_2Se_3 but result in spatially non-uniform crystallization. Longer pulses lasting 100 μs or more are necessary to crystallize the PCM uniformly [10], which justifies our pulse parameter choice here. To induce amorphization, we investigated two types of pulses, a single 8.6 V (22.4 mA), 100 ns pulse [10,19] or a 6.6 V (18.7 mA), 400 ns pulse. Both can elevate the temperature of the entire PCM-filled slot above the melting point, T_m = 620 °C (893 K). The total energy consumption for crystallization is 1.13 μJ and 21/49.4 nJ (100/400 ns pulse) for amorphization. The pulse length directly correlates with the crystallization/amorphization efficiency. Too short pulses may induce some hotspots with temperature surpassing the threshold temperature for crystallization/amorphization but fail to trigger the phase transition in other part. Figure

3-4(a) demonstrate the temperature evolution over melting-quench/annealing time resulted from a finite-element method (FEM) simulation (COMSOL Multiphysics). For the crystallization, the temperature was remained stably higher than T_c for the whole time. The 3D temperature profile predicted by thermal FEM simulation at the end of the amorphization pulse was shown in Figure 3-4(b). The 1D plot shows the whole Sb_2Se_3 slot (ranging from y = -4.25 μm to y = 4.25 μm) was elevated to above melting point, which guaranteed the complete amorphization. The 3D temperature profile predicted by thermal FEM simulation at the end of the 100 ns amorphization pulse was shown in Figure 3-4(c), suggesting that the heat is effectively confined within the target section of Sb_2Se_3. The out-of-plane temperature variation is particularly relevant for graphene heaters, given that graphene exhibits varying out-of-plane thermal resistance due to the surface polar phonons (SPoPh) scattering effect [55]. Consequently, a temperature gradient is established along the out-of-plane direction, as heat transfer occurs more efficiently towards the substrate than towards the top cladding. In order to ensure complete amorphization of Sb_2Se_3 following the melt-quenching pulse, a series of dynamic simulations was conducted with varying amorphization pulse power. Thermal FEM simulations (Figure 3-4(b)) suggest that the crystallization length within the slot barely changes at z = 0 and z = 240 nm, implying that the crystallization is uniform along the z-direction. The kinks near the two ends of the orange curve in Figure 3-4(b) are attributed to the ends of the graphene sheet.

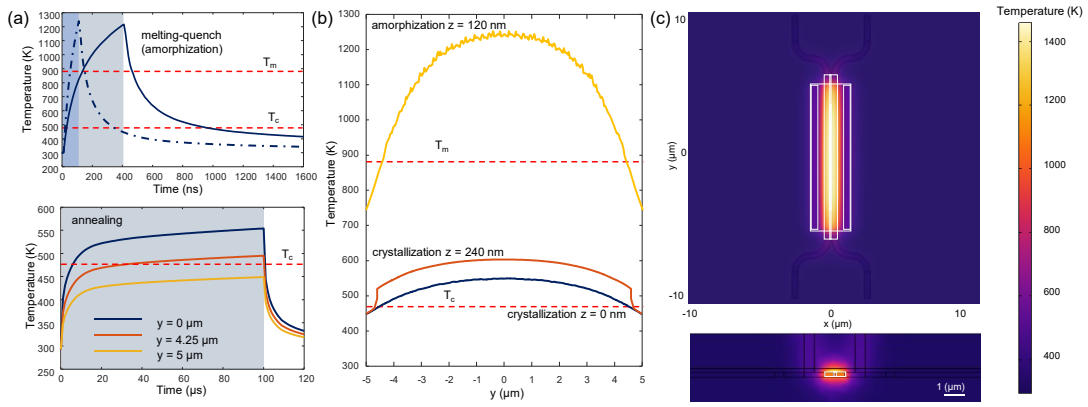

Figure 3-4. (a) FEM simulated transient temperature during and after the amorphization and crystallization pulses. The shaded areas represent pulse-on times. (b) Simulated temperature across the slot at the end of the amorphization and crystallization pulses. (c) Simulated three-dimension temperature profiles at the end of the amorphization pulse.

The quenching rate after the amorphization pulse, which is critical in gauging whether crystallization can be bypassed, is predominantly governed by thermal conductance through cladding material and BOX. As shown in Figure 3-4(a), the quenching rate is approximately 1 K/ns, which is sufficient to prohibit re-crystallization of Sb_2Se_3. As we discussed in section 2.2, the heater's geometry critically controls the area of the material to be heat up, thus, carefully optimization iteration has been done to guarantee simultaneously the required quenching rate as well as the temperature profile across the PCM slot. The required energies for amorphization and crystallization are essentially influenced by the effective heating volume. In details, as shown in Figure 3-4(c), due to the cladding, the effective heating volume of our design is about two times that of the waveguide structure with graphene heater and no cladding (Figure 2-5(b)). That can explain why the amorphization energy in this design is about two times the amorphization energy in Ref [27].

It is worth noticing the feasibility of different heater types for Sb_2Se_3 phase transition. The high melting point of Sb_2Se_3 limit the number of compatible heating materials. For example, metallic resistive heaters such as Aluminum heaters are unlikely to perform well due to the heating material's low melting point. PIN heater is suggested to be a promising option to keep the waveguide propagation loss low while being able to provide substantial heat; yet, the high voltage required during the amorphization pulses would likely to breakdown the junction. It is reported experimentally that n-doped Si heater and graphene heater successfully crystallized/amorphized optical PCMs such as Sb_2Se_3 on photonic devices [14]. In comparison with doped Si, graphene heater would have much more potential owing to its lower induced loss and higher heating efficiency [23].

Chapter 4

Conclusion and future work

Finally, we would like to discuss the scalability of our proposed photonic switch design. Thanks to its ultralow insertion loss, low power consumption and low crosstalk, the 2 × 2 switch is definitely suitable to scale up. Figure 4-1(a) demonstrates an example of 16 × 16 switch utilizing PCM multimode slots as switching elements and Figure 4-1(b) illustrate a generic scaling design for 2m × 2m switch built from 2 × 2 switch building blocks using Benes network .

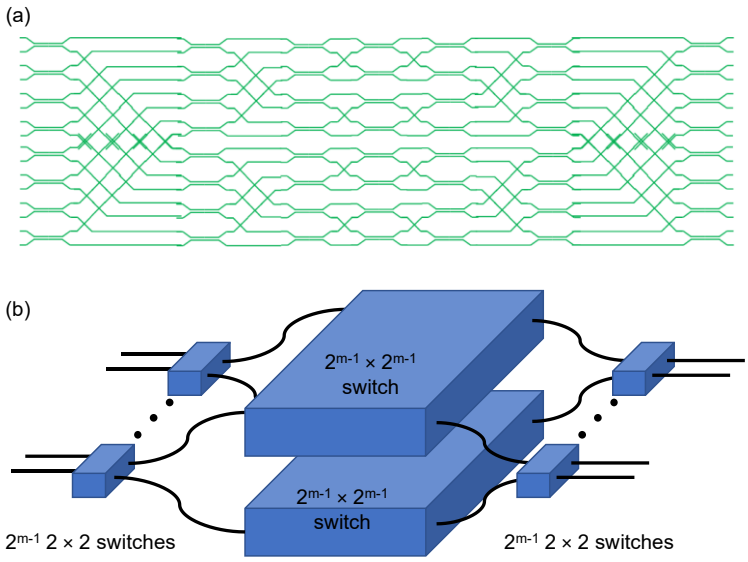

Figure 4-1. (a) Schematic for non-volatile 16 × 16 switch based on PCM phase transition. (b) Generic design for 2m × 2m switch built on 2 × 2 switch building block

Using the values presented in Table 1, we can estimate the total insertion loss and the lower and maximum crosstalk of an m-order switch matrix (assuming that the IL of a waveguide crossing in the C-band as 0.1 dB [56]):

$$IL_m = (2^m - 2) \times 0.1\ dB + (2m - 1) \times 0.45\ dB \quad (1)$$

$$CT_m = -(15\ dB - 10 \log_{10} m\ dB) \quad (2)$$

Scaling from our 2 × 2 switch's performance, a 16 × 16 switch is anticipated exhibit maximal 3.2 dB insertion loss and -24 dB crosstalk at 1550 nm, representing highly promising performance metrics, compared to the state-of-the-art (volatile) on-chip 16 × 16 switch reported by Lu et al [57]. The IL and CT scaling with network order is demonstrated in Figure 4-2.

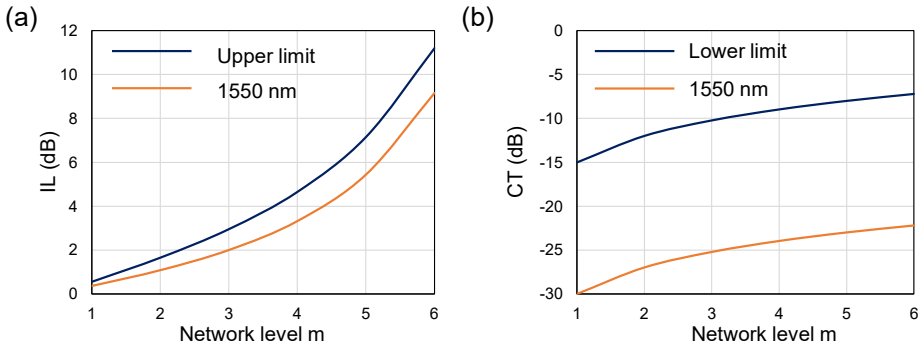

Figure 4-2. (a) Insertion loss and (b) maximum crosstalk as functions of the switch matrix of order m

The 2 × 2 switch itself can also be operated in multi-level manner by controlling the crystallization level of Sb_2Se_3. As discussed previously, the temperature distribution is not uniform over the multimode slot. Four different levels of crystallization of $Ge_2Sb_2Se_4Te_1$ (GSST) were reported to achieved by graphene heater on photonic Si_3Ni_4 platform [24]. Therefore, by controlling the power of amorphization/crystallization pulses, we can actively crystallize the slot partially and control the optical CTs.

In conclusion, we have proposed a design for compact, non-volatile, high efficiency 2 × 2 photonic switches utilizing Sb_2Se_3 and single-layer graphene heater and quantitatively analyzed its feasibility, operational parameters and performance metrics. The switch achieves exceptional compact footprint of (5.5 × 24 μm^2) with the coupling region about 6.7 times the target operational wavelength and the minimal crosstalk (-23.9 dB). The low-loss PCM Sb_2Se_3 enables a low insertion loss of 0.27 dB, and a single-layer graphene heater achieves low switching energies of 1.13 μJ for crystallization and 21 nJ for amorphization. The design showcases its scalability potential for realizing non-blocking matrix switches with arbitrarily high complexity. Furthermore, computational simulations have verified the feasibility of employing graphene heaters in integrated photonic devices, demonstrating their capability to achieve both high speed and high energy efficiency. With high speed, energy efficiency, and compact footprints, coupled

with robust optical performance, our proposed 2 × 2 switch design featuring graphene heaters provide a scalable means to control the states PCMs, which, in turn, holds the potential for the development of future large-scale PCM-based programmable PICs.

Bibliography

1. M. M. Waldrop, "The Chips Are Down for Moore's Law," Nature **530**, 144 (2016).

2. A. H. Atabaki, S. Moazeni, F. Pavanello, H. Gevorgyan, J. Notaros, L. Alloatti, M. T. Wade, C. Sun, S. A. Kruger, H. Meng, K. Al Qubaisi, I. Wang, B. Zhang, A. Khilo, C. V Baiocco, M. A. Popović, V. M. Stojanović, and R. J. Ram, "Integrating photonics with silicon nanoelectronics for the next generation of systems on a chip," Nature **556**(7701), 349–354 (2018).

3. J. Wang, S. Paesani, Y. Ding, R. Santagati, P. Skrzypczyk, A. Salavrakos, J. Tura, R. Augusiak, L. Mančinska, D. Bacco, D. Bonneau, J. W. Silverstone, Q. Gong, A. Acín, K. Rottwitt, L. K. Oxenløwe, J. L. O'Brien, A. Laing, and M. G. Thompson, "Multidimensional quantum entanglement with large-scale integrated optics," Science (1979) **360**(6386), 285–291 (2018).

4. C. Ríos, M. Stegmaier, P. Hosseini, D. Wang, T. Scherer, C. D. Wright, H. Bhaskaran, and W. H. P. Pernice, "Integrated all-photonic non-volatile multi-level memory," Nat Photonics **9**(11), 725–732 (2015).

5. D. Pérez, I. Gasulla, L. Crudgington, D. J. Thomson, A. Z. Khokhar, K. Li, W. Cao, G. Z. Mashanovich, and J. Capmany, "Multipurpose silicon photonics signal processor core," Nat Commun **8**(1), 636 (2017).

6. G. T. Reed, G. Mashanovich, F. Y. Gardes, and D. J. Thomson, "Silicon optical modulators," Nat Photonics **4**(8), 518–526 (2010).

7. C. Wang, M. Zhang, X. Chen, M. Bertrand, A. Shams-Ansari, S. Chandrasekhar, P. Winzer, and M. Lončar, "Integrated lithium niobate electro-optic modulators operating at CMOS-compatible voltages," Nature **562**(7725), 101–104 (2018).

8. C. Haffner, W. Heni, Y. Fedoryshyn, J. Niegemann, A. Melikyan, D. L. Elder, B. Baeuerle, Y. Salamin, A. Josten, U. Koch, C. Hoessbacher, F. Ducry, L. Juchli, A. Emboras, D. Hillerkuss, M. Kohl, L. R. Dalton, C. Hafner, and J. Leuthold, "All-plasmonic Mach–Zehnder modulator enabling optical high-speed communication at the microscale," Nat Photonics **9**(8), 525–528 (2015).

9. R. Chen, Z. Fang, F. Miller, H. Rarick, J. E. Fröch, and A. Majumdar, "Opportunities and Challenges for Large-Scale Phase-Change Material Integrated Electro-Photonics," ACS Photonics **9**(10), 3181–3195 (2022).

10. C. Ríos, Q. Du, Y. Zhang, C.-C. Popescu, M. Y. Shalaginov, P. Miller, C. Roberts, M. Kang, K. A. Richardson, T. Gu, S. A. Vitale, and J. Hu, "Ultra-compact nonvolatile phase shifter based on electrically reprogrammable transparent phase change materials," PhotoniX **3**(1), 26 (2022).

11. M. Wuttig, H. Bhaskaran, and T. Taubner, "Phase-change materials for non-volatile photonic applications," Nat Photonics **11**(8), 465–476 (2017).

12. P. Xu, J. Zheng, J. K. Doylend, and A. Majumdar, "Low-Loss and Broadband Nonvolatile Phase-Change Directional Coupler Switches," ACS Photonics **6**(2), 553–557 (2019).

13. J. Zheng, A. Khanolkar, P. Xu, S. Colburn, S. Deshmukh, J. Myers, J. Frantz, E. Pop, J. Hendrickson, J. Doylend, N. Boechler, and A. Majumdar, "GST-on-silicon hybrid nanophotonic integrated circuits: a non-volatile quasi-continuously reprogrammable platform," Opt Mater Express **8**(6), 1551–1561 (2018).

14. Z. Fang, R. Chen, J. Zheng, A. I. Khan, K. M. Neilson, S. J. Geiger, D. M. Callahan, M. G. Moebius, A. Saxena, M. E. Chen, C. Rios, J. Hu, E. Pop, and A. Majumdar, "Ultra-low-energy programmable non-volatile silicon photonics based on phase-change materials with graphene heaters," Nat Nanotechnol **17**(8), 842–848 (2022).

15. J. Zheng, Z. Fang, C. Wu, S. Zhu, P. Xu, J. K. Doylend, S. Deshmukh, E. Pop, S. Dunham, M. Li, and A. Majumdar, "Nonvolatile Electrically Reconfigurable Integrated Photonic Switch Enabled by a Silicon PIN Diode Heater," Advanced Materials **32**(31), 2001218 (2020).

16. F. Rao, K. Ding, Y. Zhou, Y. Zheng, M. Xia, S. Lv, Z. Song, S. Feng, I. Ronneberger, R. Mazzarello, W. Zhang, and E. Ma, "Reducing the stochasticity of crystal nucleation to enable subnanosecond memory writing," Science (1979) **358**(6369), 1423–1427 (2017).

17. R. Chen, Z. Fang, J. E. Fröch, P. Xu, J. Zheng, and A. Majumdar, "Broadband Nonvolatile Electrically Controlled Programmable Units in Silicon Photonics," ACS Photonics **9**(6), 2142–2150 (2022).

18. Y. Zhang, J. B. Chou, J. Li, H. Li, Q. Du, A. Yadav, S. Zhou, M. Y. Shalaginov, Z. Fang, H. Zhong, C. Roberts, P. Robinson, B. Bohlin, C. Ríos, H. Lin, M. Kang, T. Gu, J. Warner, V. Liberman, K. Richardson, and J. Hu, "Broadband transparent optical phase change materials for high-performance nonvolatile photonics," Nat Commun **10**(1), 4279 (2019).

19. M. Delaney, I. Zeimpekis, D. Lawson, D. W. Hewak, and O. L. Muskens, "A New Family of Ultralow Loss Reversible Phase-Change Materials for Photonic Integrated Circuits: Sb2S3 and Sb2Se3," Adv Funct Mater **30**(36), 2002447 (2020).

20. W. Dong, H. Liu, J. K. Behera, L. Lu, R. J. H. Ng, K. V. Sreekanth, X. Zhou, J. K. W. Yang, and R. E. Simpson, "Wide Bandgap Phase Change Material Tuned Visible Photonics," Adv Funct Mater **29**(6), 1806181 (2019).

21. J. Li, Y. Huang, Y. Song, L. Li, H. Zheng, H. Wang, T. Gu, K. Richardson, J. Kong, J. Hu, and H. Lin, "High-performance graphene-integrated thermo-optic switch: design and experimental validation [Invited]," Opt Mater Express **10**(2), 387–396 (2020).

22. M. Romagnoli, V. Sorianello, M. Midrio, F. H. L. Koppens, C. Huyghebaert, D. Neumaier, P. Galli, W. Templ, A. D'Errico, and A. C. Ferrari, "Graphene-based integrated photonics for next-generation datacom and telecom," Nat Rev Mater **3**(10), 392–414 (2018).

23. J. Zheng, S. Zhu, P. Xu, S. Dunham, and A. Majumdar, "Modeling Electrical Switching of Nonvolatile Phase-Change Integrated Nanophotonic Structures with Graphene Heaters," ACS Appl Mater Interfaces **12**(19), 21827–21836 (2020).

24. C. Ríos, Y. Zhang, M. Y. Shalaginov, S. Deckoff-Jones, H. Wang, S. An, H. Zhang, M. Kang, K. A. Richardson, C. Roberts, J. B. Chou, V. Liberman, S. A. Vitale, J. Kong, T. Gu, and J. Hu, "Multi-Level Electro-Thermal Switching of Optical Phase-Change Materials Using Graphene," Adv Photonics Res **2**(1), 2000034 (2021).

25. M. Stegmaier, C. Ríos, H. Bhaskaran, C. D. Wright, and W. H. P. Pernice, "Nonvolatile All-Optical 1 × 2 Switch for Chipscale Photonic Networks," Adv Opt Mater **5**(1), 1600346 (2017).

26. Q. Zhang, Y. Zhang, J. Li, R. Soref, T. Gu, and J. Hu, "Broadband nonvolatile photonic switching based on optical phase change materials: beyond the classical figure-of-merit," Opt Lett **43**(1), 94–97 (2018).

27. C. Song, Y. Gao, G. Wang, Y. Chen, P. Xu, C. Gu, Y. Shi, and X. Shen, "Compact nonvolatile 2×2 photonic switch based on two-mode interference," Opt Express **30**(17), 30430–30440 (2022).

28. S. Abdollahramezani, O. Hemmatyar, H. Taghinejad, A. Krasnok, Y. Kiarashinejad, M. Zandehshahvar, A. Alù, and A. Adibi, "Tunable nanophotonics enabled by chalcogenide phase-change materials," **9**(5), 1189–1241 (2020).

29. J. Feldmann, N. Youngblood, M. Karpov, H. Gehring, X. Li, M. Stappers, M. Le Gallo, X. Fu, A. Lukashchuk, A. S. Raja, J. Liu, C. D. Wright, A. Sebastian, T. J. Kippenberg, W. H. P. Pernice, and H. Bhaskaran, "Parallel convolutional processing using an integrated photonic tensor core," Nature **589**(7840), 52–58 (2021).

30. C. Wu, H. Yu, S. Lee, R. Peng, I. Takeuchi, and M. Li, "Programmable phase-change metasurfaces on waveguides for multimode photonic convolutional neural network," Nat Commun **12**(1), 96 (2021).

31. Q. Wang, E. T. F. Rogers, B. Gholipour, C.-M. Wang, G. Yuan, J. Teng, and N. I. Zheludev, "Optically reconfigurable metasurfaces and photonic devices based on phase change materials," Nat Photonics **10**(1), 60–65 (2016).

32. M. Y. Shalaginov, S. D. Campbell, S. An, Y. Zhang, C. Ríos, E. B. Whiting, Y. Wu, L. Kang, B. Zheng, C. Fowler, H. Zhang, D. H. Werner, J. Hu, and T. Gu, "Design for quality: reconfigurable flat optics based on active metasurfaces," **9**(11), 3505–3534 (2020).

33. F. Yang, K. P. Dao, S. An, X. Qiu, Y. Zhang, J. Hu, and T. Gu, "Design of continuously tunable varifocal metalenses," Journal of Optics **25**(11), 115102 (2023).

34. M. N. Julian, C. Williams, S. Borg, S. Bartram, and H. J. Kim, "Reversible optical tuning of GeSbTe phase-change metasurface spectral filters for mid-wave infrared imaging," Optica **7**(7), 746–754 (2020).

35. C. Ruiz de Galarreta, I. Sinev, A. M. Alexeev, P. Trofimov, K. Ladutenko, S. Garcia-Cuevas Carrillo, E. Gemo, A. Baldycheva, J. Bertolotti, and C. David Wright, "Reconfigurable multilevel control of hybrid all-dielectric phase-change metasurfaces," Optica **7**(5), 476–484 (2020).

36. Q. Tan, Y. Chang, Q. He, H. Tong, and X. Miao, "Enhanced stretchability towards a flexible and wearable reflective display coating using chalcogenide phase change materials," Opt Express **31**(1), 75–85 (2023).

37. Z. Ni, S. Mou, T. Zhou, and Z. Cheng, "Broader color gamut of color-modulating optical coating display based on indium tin oxide and phase change materials," Appl Opt **57**(13), 3385–3389 (2018).

38. P. Hosseini, C. D. Wright, and H. Bhaskaran, "An optoelectronic framework enabled by low-dimensional phase-change films," Nature **511**(7508), 206–211 (2014).

39. M. Y. Shalaginov, S. An, Y. Zhang, F. Yang, P. Su, V. Liberman, J. B. Chou, C. M. Roberts, M. Kang, C. Rios, Q. Du, C. Fowler, A. Agarwal, K. A. Richardson, C. Rivero-Baleine, H. Zhang, J. Hu, and T. Gu, "Reconfigurable all-dielectric metalens with diffraction-limited performance," Nat Commun **12**(1), 1225 (2021).

40. Y. Zhang, C. Fowler, J. Liang, B. Azhar, M. Y. Shalaginov, S. Deckoff-Jones, S. An, J. B. Chou, C. M. Roberts, V. Liberman, M. Kang, C. Ríos, K. A. Richardson, C. Rivero-Baleine, T. Gu, H. Zhang, and J. Hu, "Electrically reconfigurable non-volatile metasurface using low-loss optical phase-change material," Nat Nanotechnol **16**(6), 661–666 (2021).

41. H. Y. Lee, S. Moon, S. J. Park, J. Lee, K. H. Park, and J. Kim, "Micro-machined resistive micro-heaters for high temperature gas sensing applications," Electron Lett **44**(25), 1460–1461 (2008).

42. Y. Wu, X. Du, Y. Li, H. Tai, and Y. Su, "Optimization of temperature uniformity of a serpentine thin film heater by a two-dimensional approach," Microsystem Technologies **25**(1), 69–82 (2019).

43. Y. Zhang, C. Ríos, M. Y. Shalaginov, M. Li, A. Majumdar, T. Gu, and J. Hu, "Myths and truths about optical phase change materials: A perspective," Appl Phys Lett **118**(21), 210501 (2021).

44. P. K. Khulbe, E. M. Wright, and M. Mansuripur, "Crystallization behavior of as-deposited, melt quenched, and primed amorphous states of Ge2Sb2.3Te5 films," J Appl Phys **88**(7), 3926–3933 (2000).

45. J. D. Musgraves, J. Hu, and L. Calvez, *Springer Handbook of Glass*, 1st ed (Springer International Publishing, 2019).

46. B.-S. Lee, R. M. Shelby, S. Raoux, C. T. Retter, G. W. Burr, S. N. Bogle, K. Darmawikarta, S. G. Bishop, and J. R. Abelson, "Nanoscale nuclei in phase change materials: Origin of different crystallization mechanisms of Ge2Sb2Te5 and AgInSbTe," J Appl Phys **115**(6), 063506 (2014).

47. C. Rios, M. Stegmaier, Z. Cheng, N. Youngblood, C. D. Wright, W. H. P. Pernice, and H. Bhaskaran, "Controlled switching of phase-change materials by evanescent-field coupling in integrated photonics [Invited]," Opt Mater Express **8**(9), 2455–2470 (2018).

48. Y. K. Lee, C. Yoo, W. Kim, J. W. Jeon, and C. S. Hwang, "Atomic layer deposition of chalcogenides for next-generation phase change memory," J Mater Chem C Mater **9**(11), 3708–3725 (2021).

49. Rashi Sharma, Casey Schwarz, Daniel Wiedeman, Eric Bissel, Brian Mills, Marie Sykes, Jasper Stackawitz, Jake Klucinec, Dennis Callahan, JueJun Hu, Parag Banerjee, and Kathleen Richardson, "Solution-Based Sb2Se3 Thin Films for Microphotonics ," (Submitted) (2023).

50. J.-Y. Hong, Y. C. Shin, A. Zubair, Y. Mao, T. Palacios, M. S. Dresselhaus, S. H. Kim, and J. Kong, "A Rational Strategy for Graphene Transfer on Substrates with Rough Features," Advanced Materials **28**(12), 2382–2392 (2016).

51. X. Yang, M. S. Nisar, W. Yuan, F. Zheng, L. Lu, J. Chen, and L. Zhou, "Phase change material enabled 2 × 2 silicon nonvolatile optical switch," Opt Lett **46**(17), 4224–4227 (2021).

52. C. Zhang, M. Zhang, Y. Xie, Y. Shi, R. Kumar, R. R. Panepucci, and D. Dai, "Wavelength-selective 2 × 2 optical switch based on a Ge2Sb2Te5-assisted microring," Photonics Res **8**(7), 1171–1176 (2020).

53. C. Wu, H. Yu, H. Li, X. Zhang, I. Takeuchi, and M. Li, "Low-Loss Integrated Photonic Switch Using Subwavelength Patterned Phase Change Material," ACS Photonics **6**(1), 87–92 (2019).

54. M. Delaney, I. Zeimpekis, H. Du, X. Yan, M. Banakar, D. J. Thomson, D. W. Hewak, and O. L. Muskens, "Nonvolatile programmable silicon photonics using an ultralow-loss Sb2Se3 phase change material," Sci Adv **7**(25), eabg3500 (2023).

55. X. Tang, S. Xu, J. Zhang, and X. Wang, "Five Orders of Magnitude Reduction in Energy Coupling across Corrugated Graphene/Substrate Interfaces," ACS Appl Mater Interfaces **6**(4), 2809–2818 (2014).

56. L. Qiao, W. Tang, and T. Chu, "32 × 32 silicon electro-optic switch with built-in monitors and balanced-status units," Scientific Reports 2017 7:1 **7**(1), 1–7 (2017).

57. L. Lu, S. Zhao, L. Zhou, D. Li, Z. Li, M. Wang, X. Li, and J. Chen, "16 × 16 non-blocking silicon optical switch based on electro-optic Mach-Zehnder interferometers," Opt Express **24**(9), 9295–9307 (2016).